Extensions to the charge exchange recombination spectroscopy diagnostic suite at ASDEX Upgrade

R. M. McDermott,[1, a)] A. Lebschy,[1, 2] B. Geiger,[3] C. Bruhn,[1, 2] M. Cavedon,[1] M. Dunne,[1] R. Dux,[1] R. Fischer,[1] A. Kappatou,[1] T. Pütterich,[1] E. Viezzer,[4] and the ASDEX Upgrade Team[5, b)]

[1)] *Max-Planck-Institut für Plasmaphysik Boltzmannstr. 2, 85748 Garching, Germany*

[2)] *Physik-Department E28, Technische Universität München, D-85748 Garching, Germany*

[3)] *Max-Planck-Institut für Plasmaphysik,Wendelsteinstr. 1, 17491 Greifswald, Germany*

[4)] *Dept. of Atomic, Molecular and Nuclear Physics, University of Seville, Avda. Reina Mercedes, 41012 Seville, Spain*

[5)] *Max-Plank-Institut für Plasmaphysik, D-85748, Garching, Germany*

(Dated: 11 July 2017)

A new core charge exchange recombination spectroscopy (CXRS) diagnostic has been installed in the ASDEX Upgrade tokamak that is capable of measuring the impurity ion temperature, toroidal rotation, and density on both the low field side (LFS) and high field side (HFS) of the plasma. The new system features 48 lines-of-sight (LOS) with a radial resolution that varies from ± 2cm on the LFS down to ± 0.75cm on the HFS and has sufficient signal to run routinely at 10ms and for special circumstances down to 2.5ms integration time. The LFS-HFS ion temperature profiles provide an additional constraint on the magnetic equilibrium reconstruction and the toroidal rotation frequency profiles are of sufficiently high quality that information on the poloidal velocity can be extracted from the LFS-HFS asymmetry. The diagnostic LOS are coupled to two flexible-wavelength spectrometers such that complete LFS-HFS profiles from two separate impurities can be imaged simultaneously, albeit with reduced radial coverage. More frequently, the systems measure the same impurity providing very detailed information on the chosen species. Care has been taken to calibrate the systems as accurately as possible and to include in the data analysis any effects that could lead to spurious temperatures or rotations.

---

[a] Electronic mail: Rachael.McDermott@ipp.mpg.de
[b] For authors' list, see H. Zohm et al., NF 55 104010 (2015)

I. INTRODUCTION

Charge exchange recombination spectroscopy (CXRS) is a routine diagnostic on most fusion experiments to measure the temperature, rotation and density of impurity ions (typically low-Z) in the plasma[1,2]. The technique relies on the transfer of electrons from neutral particles to impurity ions, which subsequently de-excite and emit characteristic line radiation (the measured CX spectra). In most fusion plasmas, due to the high temperature and densities, the natural population of neutral particles is extremely low making the charge exchange signal negligibly small. However, if a population of neutral particles is introduced into the plasma via a gas puff, a neutral beam, or a pellet then the charge exchange signal can become sufficiently large to diagnose the impurity temperature and rotation from the Doppler width and shift of the measured emission line and the impurity density from the measured intensity coupled with knowledge of the neutral particle population. In addition, the injection of a population of neutral particles yields the added benefit of localizing the CXRS measurements to the intersection of the lines-of-sight (LOS) with the cloud of neutral particles.

Regardless of the source, the number of neutral particles decreases with distance into the plasma due to ionisation and charge exchange processes and the measured CXRS signal decreases accordingly. For this reason, and often for geometry and hardware considerations, CXRS systems in fusion devices have traditionally focused on measurements in the outer half of the plasma, in tokamaks the so-called low field side (LFS), and relied on the assumption that these parameters are constant on magnetic flux surfaces to map them to other locations in the plasma. This was the situation, for example, at ASDEX Upgrade (AUG) until recently[3].

Similar to systems existing at TCV[4] and DIII-D[5], a new core CXRS diagnostic capable of measuring across the magnetic axis of the machine and providing both LFS and high field side (HFS) measurements was implemented at ASDEX Upgrade for the 2014 experimental campaign. This system is capable of providing up to 48 point CXRS profiles across the mid-plane of the plasma from the pedestal top on the LFS to the pedestal top on the HFS with high temporal and radial resolution. This is possible due to a combination of improved optical design of the in-vessel system, low f-number spectrometers, and high neutral beam energy (93 keV). With this system, impurity ion temperature, rotation and density profiles

can be obtained at two different positions on a magnetic flux surface, thus enabling the study of poloidal asymmetries in these quantities and the determination of the poloidal flow in the core plasma[4–6].

This paper is organized as follows: In section II the design, geometry, and hardware of the new LFS-HFS CXRS diagnostics are presented. The details of the calibrations of these systems are given in III. Section IV demonstrates the capabilities of the new systems, showing examples of the measured spectra and deduced impurity ion temperature, rotation and impurity density profiles. Charge exchange cross-section effects and the effects of other atomic processes on the measured CXRS spectra are discussed in section V and, finally, a summary of this work is presented in section VI.

II. NEW CXRS DIAGNOSTICS

AUG is equipped with two neutral beam boxes separated toroidally by 180 degrees. Each box is comprised of four sources capable of delivering 2.5MW of power each (in D) for a total of 20MW of available neutral beam injection (NBI) power. The beam boxes have maximum acceleration voltages of 60 keV (box I, sources 1-4) and 93 keV (box II, sources 5-8) and the majority of the pre-existing CXRS diagnostics utilise source 3 of NBI box I. This has the advantage that the inclusion of just one NBI source in a plasma discharge enables measurements from the complete suite of CXRS diagnostics. However, this has occasionally been problematic as CXRS measurements were not available when beam box I was not in operation due to technical reasons or the constraints of a given experiment. For this reason, it was decided that the new CXRS diagnostics would view one of the sources from beam box II.

In addition, NBI box II provides a second advantage with respect to box I. Namely, the higher energy beam suffers less from attenuation leading to improved CXRS signals in the plasma core and on the HFS. While both neutral beam boxes deliver the same power, the sources in box II inject fewer neutral particles in comparison to box I, due to the differences in acceleration voltage. This would lead to a reduction in the CXRS signal, except the lower particle numbers are very well compensated (to within ∼10%) by the increase in the CXRS cross-sections, which peak around 100keV (∼50keV/amu) for most of the standard CXRS transitions (e.g. B n=7-6, C n=8-7) . Therefore, the CXRS systems viewing the 60keV and
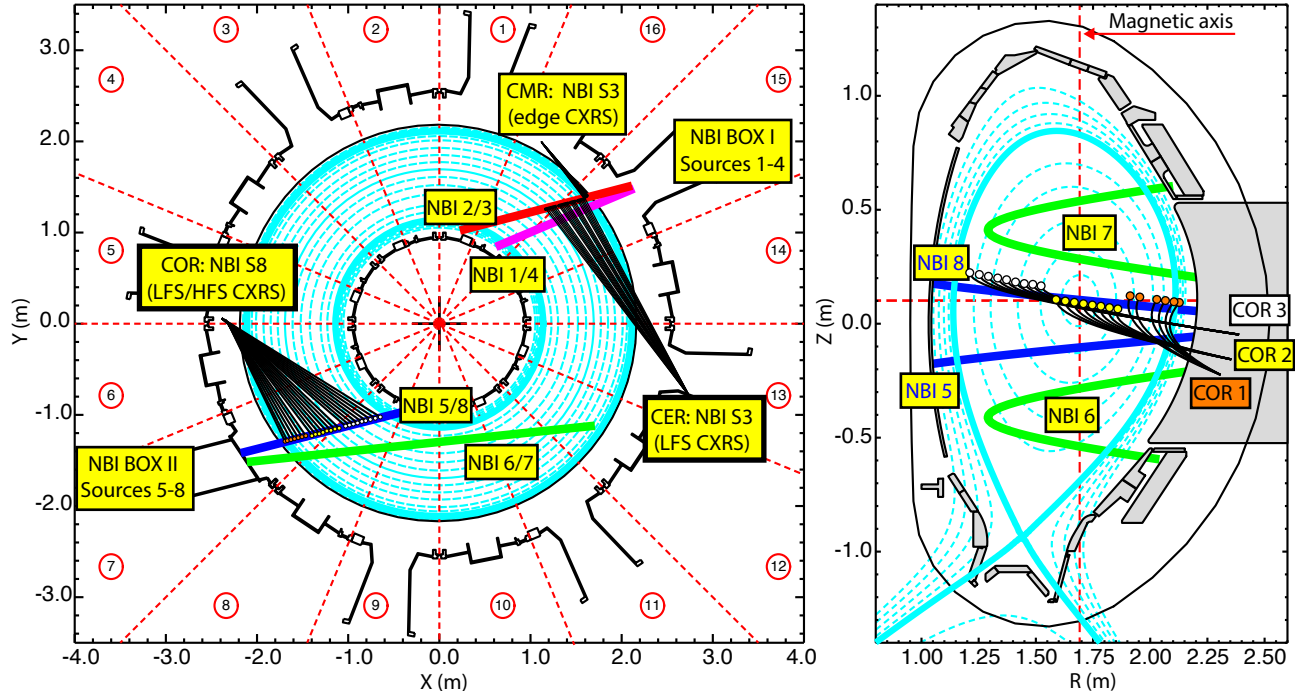
FIG. 1. Top-down (left) and poloidal (right) cross-sections of AUG showing the geometries of the NBI sources as well as a subset of the LOS of the core and edge toroidal CXRS diagnostics. For clarity, only sources from NBI box II and a subset of the LOS from the new diagnostics are shown in the poloidal projection. The equilibrium is taken from discharge 33096 at 2s.

93KeV NBI sources see very similar intensities at the plasma LFS edge. With distance into the core, however, the higher energy of box II provides an advantage.

The geometries of the four neutral beam sources in NBI box II are shown in Fig. 1. Sources 5 and 8 are injected radially with small, symmetric vertical tilts above and below the mid-plane of the machine. Sources 6 and 7 are injected tangentially significantly above and below the mid-plane. A standard magnetic equilibrium of an AUG plasma is over-plotted in light blue. From the poloidal cross-section one can see that the center point of the plasma is (often) positioned at slightly positive Z-values making NBI 8 the only NBI source of box II that can support CXRS measurements in the plasma core.

Taking this into account, three new optical heads comprising the COR diagnostic have been installed between sectors 5 and 6 and are aligned such that the entire path-length of NBI 8 in the plasma volume can be imaged. A subset of the LOS from these optical heads is shown in Fig. 1. Fig. 2 shows the design drawings as well as the manufactured optical
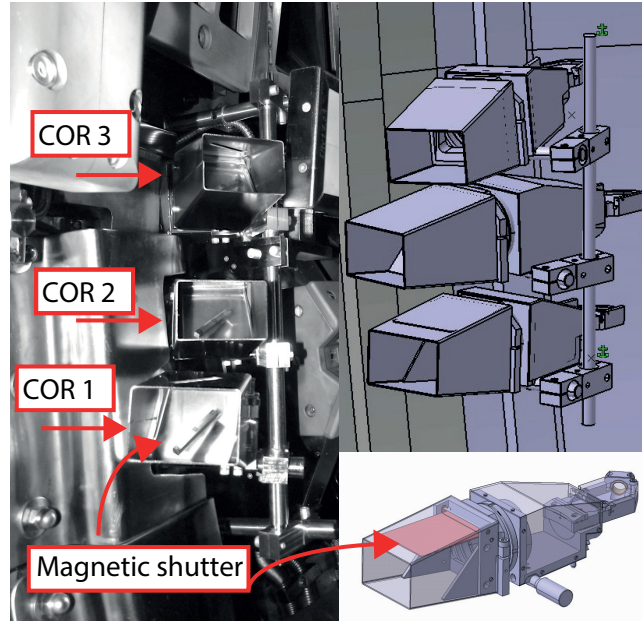
FIG. 2. Three new optical heads have been installed in the AUG vacuum vessel between sectors 5 and 6 behind the adjacent limiter shadow. A photograph of the optical heads in shown on the left, while on the right techincal drawings for these heads are shown.

heads installed in the vessel. COR 1 is equipped with 20 fibre optics and images the LFS of the plasma from a major radius of 1.89m to 2.13m. The second optical head, COR 2, with 23 lines of sight, covers the plasma centre from 1.57m to 1.86m and is shifted vertically downward (away from the centre of source 8) by several centimetres in order to obtain better coverage across the magnetic axis of the plasma. Lastly, COR 3 has 27 fibres and covers the HFS from R=1.2m to 1.54m. Together these three heads provide 70 measurement positions across the full minor radius of the plasma (pedestal top to pedestal top) with a channel to channel separation of roughly 1.5 cm.

The optical heads employ a fairly simple design in which a single aspherical lens with a 50mm diameter and 80mm focal length (F/1.6) is used to focus the light from the plasma onto an array of 400μ (F/2.2) silica-clad-silica fiber optics arranged at the focal distance behind the lens. The aspherical lenses were found to have improved imaging properties with respect to similar plano-convex lenses resulting in sharper images and improved radial resolution. A comparison of the images produced using the two lenses is shown in Fig. 3. Here, diodes were used to measure the light intensity across the diameter of the image. The vertical axis shows the measured current in the diode. The radial region from which light
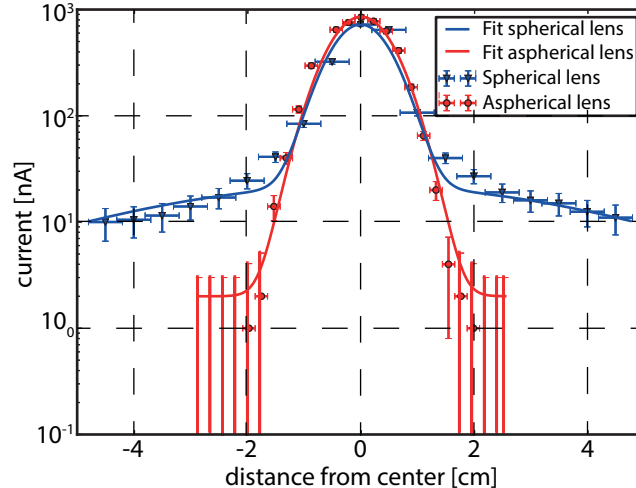
FIG. 3. Comparison of spot-size using a spherical and aspherical lens for the new CXRS diagnostic design. The aspherical lenses improve the focus and reduces the effective spot-size to 1.5cm.

is collected is significantly reduced when using the aspherical lenses leading to an effective spot-size of 1.5 cm. In the vessel, the lens of each head is protected from glow discharges and boronizations by a magnetic shutter actuated by a piece of iron welded to each lens cover and oriented such that when a toroidal magnetic field is present the shutters are pulled open and otherwise remain closed. The orientation was chosen such that the shutters will open for both forward and reversed field magnetic configurations. These shutters, visible in Fig. 2, were also tested in the lab prior to installation to ensure that they would open even for the lowest toroidal magnetic fields employed in the AUG tokamak ($\sim$ 1T).

The LOS geometries of all of the fibers in the optical heads are determined to high accuracy by back-lighting the fibre optics and measuring the intersection coordinates of the LOS with planar surfaces (specifically installed for this purpose) with a robotic arm and a three-dimensional model of the AUG vacuum vessel. Multiple positions are measured along each LOS enabling the geometry and optical head positions to be determined to an accuracy of $\sim$1mm. Here, the "optical head" position refers to the position at which all of the LOS from a given head converge. This information is then used to determine the measurement positions and spatial resolution as well as the angles of the LOS to the magnetic field lines and to the NBI trajectories. The measured charge exchange intensities are proportional to the sum of the neutral particle populations integrated along the LOS, weighted by the corresponding effective emission rate, see Eqn. 1.

$$L_{CX,Z}(\lambda) \propto n_Z \sum_n \sum_j \langle \sigma_{n,j,Z,\lambda} v_j \rangle_{eff} \int_{LOS} n_{0,n,j}(l)\, dl \tag{1}$$

Here, L is the measured charge exchange intensity for a particular element, Z, and transition wavelength, λ, and n_Z is the impurity density, which is assumed to be constant along the intersection of the LOS and the neutral beam. The summations on n and j are over the principle quantum number of the donor neutral and the neutral beam energy components, respectively, and $\langle \sigma_{n,j,Z,\lambda} v_j \rangle_{eff}$ is the appropriate effective emission rate with σ the charge exchange cross-section and v_j the collision velocity. The effective position of the CXRS measurement is then given by the center of mass of the total distribution along the LOS as a function of R and Z. For the AUG beams, the neutral distributions of the different energy components and excited states have slightly different divergences along the beam. However, the differences are quite small and the CXRS intensity (for NBI Box 2) is dominated by the ground state of the first energy component. Therefore, the effective measurement positions are typically calculated using only the neutral distribution from this component of the beam.

$$R_{COM} = \frac{\int_{LOS} R_{LOS} n_{0,0,0}(l)\, dl}{\int_{LOS} n_{0,0,0}(l)\, dl} \tag{2}$$

This has also been compared to calculations using all energy components and excited states and been found to be the same well within the error bars on the calculations. Please note that for the purposes of these calculations $n_{0,n,j}$ is modelled using a beam attenuation code, which requires a magnetic equilibrium in order to map the necessary plasma profiles (n_e, T_e, T_i) onto the LOS positions. In all cases a standard AUG magnetic equilibrium has been used. In principle, the determined measurement positions can change slightly for different plasma shapes, positions, and parameters. However, due to AUG's relatively limited shaping capability, these corrections are also well within the error bars for the vast majority of AUG plasmas. Small changes in the three dimensional model for the neutral beam trajectories used for the calculations, however, can make a significant impact on the calculated measurement positions. The beam model used in this work has been constrained by beam emission spectroscopy (BES) measurements and images of the beam impact on the inner wall of the machine. All of the neutral beams at AUG have a full width half maximum of approximately 20cm. Care has been taken to ensure that the grids used for the neutral density integrals along the LOS encompass the entire beam (typically 80cm in

the directions perpendicular to the beam trajectory) and are sufficiently dense to describe the beam geometry well (∼1.5cm resolution perpendicular to the beam).

Examples of the LOS integrals through the beam as a function of major radius are shown in the top row of Fig. 4 for three LOS corresponding to the centre fiber from each optical head. Magenta arrows indicate the direction along the LOS away from the optical head position. The centre of mass of each distribution is shown by a red dashed line and the radial and vertical error bars are taken at the positions encompassing 67% of the total neutral distribution. In the bottom row the radial and vertical error bars for all 70 LOS are shown.

The LOS from the innermost two heads are very tangent to magnetic flux surfaces yielding a radial spread of signal less than 1cm after integrating through the neutral beam. Therefore, for these LOS, the radial resolution is effectively determined by the spot-size of the optics (±0.75cm). The LOS from COR 1 (the LFS head) are less tangential and the integration yields radial resolutions of up to ±2cm at the edge. Error bars on the Z-positions of the measurements are similar for all LOS, ∼ ±1.6cm. The radial and vertical error bars of these systems are included in the analysis of the data whenever the profiles are mapped via magnetic flux surfaces. On the HFS, the different NBI sources in box II are well separated vertically and the LOS only measured emission from NBI source 8. On the LFS, however, some emission from NBI sources 5 and 7 is also observed and is taken into account in the calculated radial positions of the measurements, radial resolution, and in the analysis of the impurity densities when these beams sources are in use.

Of the 70 LOS from the three optical heads, 48 LOS are dedicated to CXRS measurements. The remaining 22 LOS are dedicated to BES measurements, which are important to the CXRS systems for two reasons. First, the BES measurements help to constrain the three dimensional geometries used to describe the beams and calculate the effective measurement positions. Second, accurate knowledge of the absolute neutral densities of all of the beam energy components and excited states is needed to determine impurity densities from the CXRS measurements. BES measurements of the D_α spectrum provide a measurement of the n=3 populations of all beam energy components. With the help of a radiative model, this can be translated into LOS integrated measurements of the neutral densities in the ground and first excited state[7,8]. This information is exactly what is needed to calculate CXRS impurity densities, see Eqn. 1, and can also be used to benchmark the neutral density
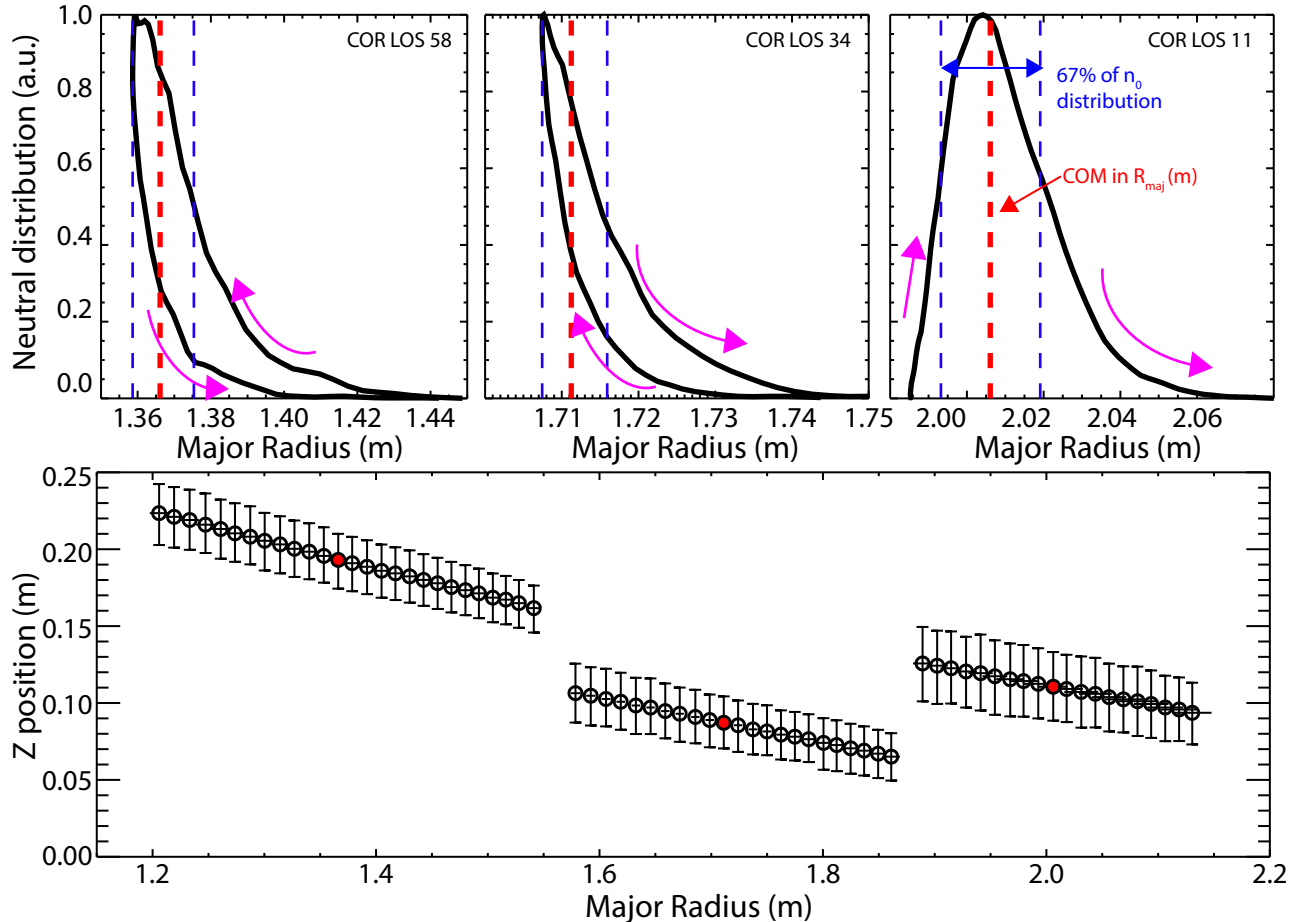
FIG. 4. In the top row the neutral density distributions as a function of radial position along a LOS for a central channel from each optical head are shown. The centre of mass of each distribution is indicated by the red dashed line and the blue dashed lines indicate the radial region containing 67% percent of the neutral distribution. Magenta arrows indicate the direction along the LOS away from the optical head position. The (R,Z) coordinates of all 70 LOS are shown in the bottle panel. The red measurement positions corresponds to the LOS integral shown in the top panels.

distributions calculated via attenuation codes. The BES system and the analysis of the BES data will be described in more detail in a separate publication.

For the CXRS measurements two identical, dedicated spectrometers have been designed and built, see Fig. 5. These spectrometers (dubbed COR and CUR) are very similar to those presented in Viezzer *et al*[3], but have some notable modifications. The new systems feature larger objective lenses reducing the total $F/\#$ of the system from 4 to 2.8 and introducing roughly a factor of two more light. To accommodate these lenses the spectrometers
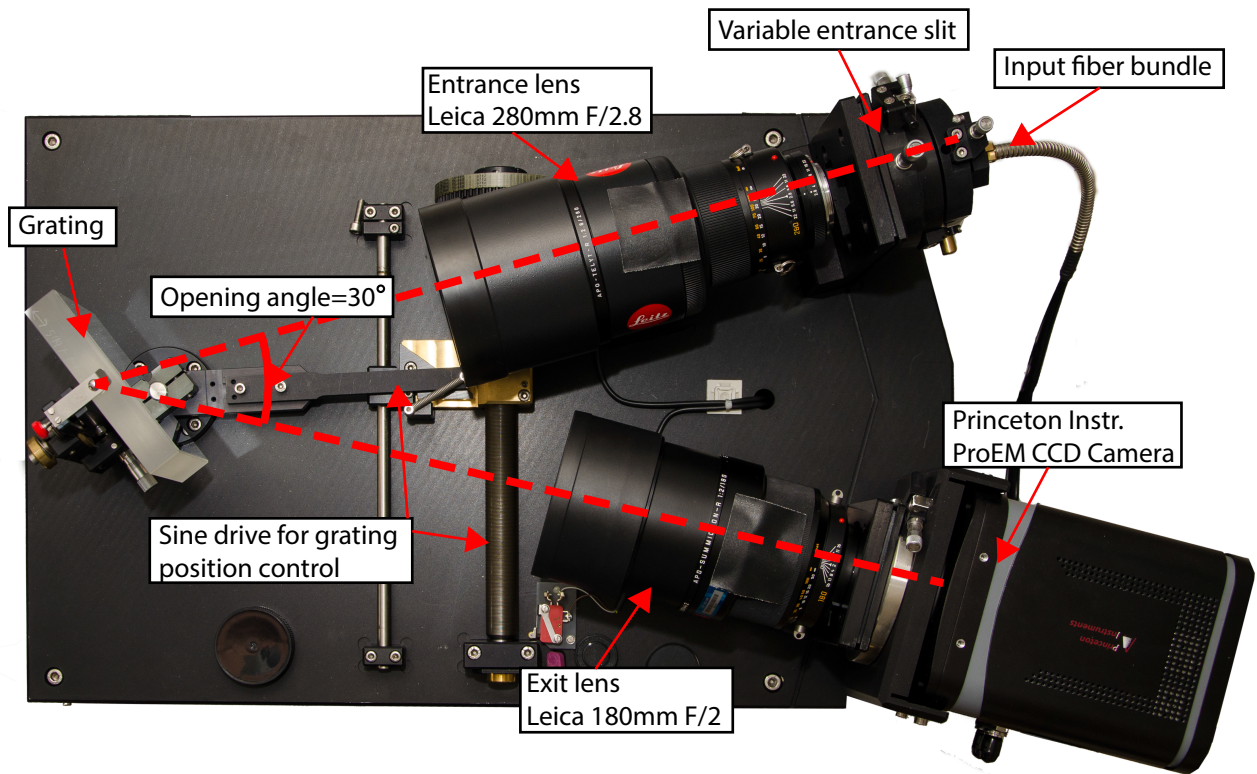
FIG. 5. Top-down view of the COR spectrometer including all optical components.

have larger opening angles (30° opposed to 20°) and a larger grating (104x112 mm) with 2400grooves/mm. To parallelize the incoming light onto the grating, Leica lenses with $F/2.8$ and focal lengths of 280mm are used at the entrance to the spectrometers. At the exit, to refocus the diffracted light, Leica lenses with $F/2.0$ and 180mm focal lengths are used. The difference in the focal lengths of the entrance and exit lenses introduces a demagnification factor of 1.56 and enables the 25 vertically stacked optical fibers at the entrance slit to be imaged without overlap on the 512×512 16 μm CCD chip[9]. For each fiber, a fixed region in pixel space is defined and binned together (perpendicular to the wavelength direction) before being read out at 10MHz, thus speeding up the readout of the camera by a factor of 20. These binned regions per fiber are referred to in subsequent text as the 'channels' of the spectrometer.

The minimum integration time of the cameras with 25 channels is 2.41ms. However, the systems are often signal-limited to longer integration times. Typically, the systems can be

operated with a 10ms integration time while still providing good quality measurements on both the LFS and the HFS. For special circumstances, such as low density plasmas, fresh boronization, and impurity seeding (of the measured impurity) it is possible to operate the systems at lower integration time.

III.   SYSTEM CALIBRATIONS

In order to extract useful information on the impurity ion temperature, rotation, and density, the systems must be absolutely calibrated. These calibrations include the instrument functions of the spectrometers, the dispersion on the cameras, wavelength calibrations, noise, gain, and smear characterisation, and the absolute intensity calibrations of the entire systems. Information on these calibrations is presented in this section.

For the new systems, the widths of the entrance slits in front of the fibers is variable, enabling a balance to be struck between the amount of light collected and the width and shape of the resultant instrument functions. For standard operation a slit width of $100\mu m$ was chosen. This setting was found to be sufficient in terms of signal, however, the instrument functions are not well described by single Gaussians, see Fig. 6. This instrument function corresponds to a central channel of the COR spectrometer. The instrument functions for the other channels of the COR and CUR spectrometers are very similar. Fortunately, for all AUG plasmas the ion temperature is high enough that the line broadening of the measured spectra is dominated by Doppler broadening and no differences in the measured rotations or temperatures have been observed when using a Gaussian approximation to the instrument function instead of the full instrument function line shape. Therefore, in the analysis of the CX data within the fitting code CXSFIT[10] a single Gaussian approximation to the instrument function is used. However, accounting for the non-Gaussian line shape was found to be important for defining and maintaining the wavelength calibrations of the systems to the desired accuracy (< 1km/s), as described below. The exact instrument function for each channel was characterized as a function of wavelength using spectral lines from neon pen lamps.

The vertical displacement of the fibres at the spectrometer entrance away from the optical axis of the system results in a parabolic distribution of the central wavelength in the vertical direction[11] and small damages to and mis-alignments of the fibers at the entrance slit result

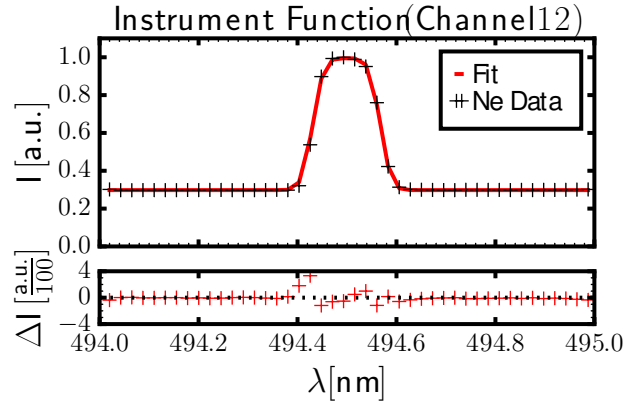Instrument Function(Channel12)

FIG. 6. Example of a non-Gaussian instrument function measured on channel 12 of the COR spectrometer. The spectral line is a neon I line at 494.498nm. This line, in addition to others, is used to characterize the instrument functions and wavelength calibrations around the boron n=7-6 charge exchange transition at 494.467nm.

in deviations of the position of the central wavelength away from this curve as shown in Fig. 7. These positions have been measured for all channels as a function of wavelength using neon lamps. With this information, an exact wavelength position measured on one channel is sufficient to know the wavelength calibrations for the entire camera. Therefore, one channel on each camera is dedicated to neon wavelength calibrations, which are performed automatically after each plasma discharge. This enables the wavelength measured by the spectrometers, and hence the impurity measured, to be changed on a shot-to-shot basis without reducing the accuracy of the wavelength calibrations. Typically, both spectrometers are set to measure the same impurity (B or N) providing very detailed measurements of a single impurity. However, thanks to the flexibility of the systems, the two systems can provide complete profiles of two separate impurities, albeit with reduced radial coverage.

An example fit to the full neon spectrum measured on the COR spectrometer centered at 495nm is shown in Fig. 8. At this wavelength, 11.4nm are imaged on the camera giving a mean dispersion of 0.022nm/pixel, making a one pixel shift the equivalent of 13km/s. Here, the entire spectrum is fit yielding a wavelength correction for the camera of 0.0356nm, which corresponds to 21 km/s. The uncertainty on the wavelength position is 0.0005nm or 0.3 km/s. The exact shape of the instrument function for the fit and the exact relationship between the COM of this instrument function compared to the others is important for
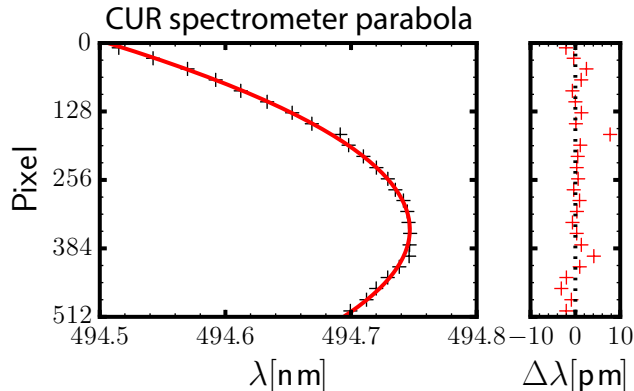
FIG. 7. Measured positions of the neon I line at 494.498nm with respect to the wavelength axis of the top-most channel of the CUR spectrometer. The red line is the theoretical position based on the vertical displacement of each channel (optical fiber) away from the optical axis of the camera. Deviations of the measured position away from the fit are measured as a function of wavelength and included in the wavelength calibrations. For this camera, the optical axis of the system is not centered on the chip.
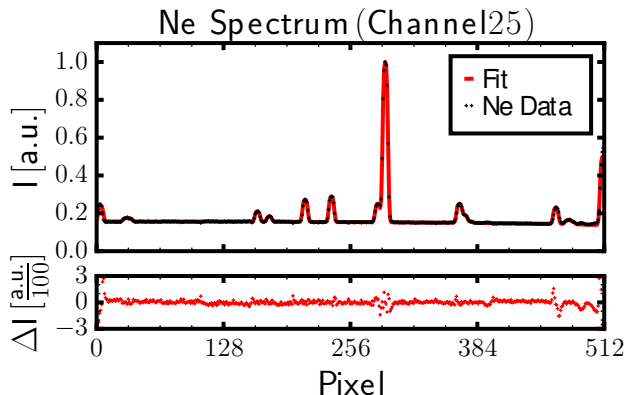

FIG. 8. Fit to the neon spectrum centred at 495nm after discharge 32866. Here, the position of each line in the spectra is reproduced by the fit to within 0.0005nm yielding an uncertainty on the central wavelength of 0.3km/s

maintaining the channel to channel relative wavelength calibration to better than 1km/s.

Princeton Instrument ProEm EMCCD[9] cameras with both standard ADC gain as well as avalanche (EM) gain are used for these systems. As the gain settings used in the experiments vary depending on signal levels and desired exposure times, all of the gain settings

and combination of ADC and EM gains have been characterised for each camera using a calibrated integrating sphere. The read-out noise and photon noise for the cameras have also been characterised and used to calculate the uncertainty on the intensity per pixel, which enters into the fits to the spectrum. The background on the camera is measured with additional frames of the same integration time as used in the experiment after every plasma discharge and the smear on the camera due to the reading out of the chip while it remains exposed to plasma light (no shutters are used) is measured during the plasma discharge on the channel reserved for the neon calibrations.

The intensity sensitivities of the systems, which are needed to calculate absolute impurity densities from the measured CXRS line intensities, are also absolutely calibrated. The fiber optics of the systems are not continuous from the optical heads to the spectrometer. Rather, the optical head fibres connect to relay fibres, which in turn connect to the spectrometer fibers. The connections between the optical head fibers and the relay fibers are fixed and, therefore, these two pieces of the systems are always considered together. The connections between the relay fibers and the spectrometer fibers, however, are not fixed and are disconnected regularly in between experimental campaigns to allow complete calibration of the spectrometers. With this setup, it is possible to connect the fiber optic for a particular LOS to any channel of any spectrometer and to change the arrangement of the fiber optics connections during the campaign. In practice, however, this is not done. It is found that the absolute intensity calibration of a LOS is only reproduced to within 10-15% if the fiber coupling is changed. Therefore, the absolute intensity calibrations are done with the fiber optics connected to a dedicated position on a spectrometer and this coupling remains fixed for the entire experimental campaign. The CXRS LOS from the three new optical heads were evenly divided between the COR and CUR spectrometers such that each spectrometer can independently provide complete LFS-HFS CXRS profiles, see Fig. 11. This way it is possible to measure complete CXRS profiles from two different low-Z impurities simultaneously or to make very detailed profile measurements of a single species. Additionally, this arrangement enables an easy cross-check of the intensity and wavelength calibrations of the two spectrometers by comparing the measured profiles.

The intensity calibrations of the entire systems are done by filling the acceptance cones of the optical heads inside the vessel with a calibrated integrating sphere[12] and measuring the resulting count rates on the cameras as a function of wavelength from 400nm to 700nm.

Unfortunately, this is only possible before and after experimental campaigns when access to the torus is possible. Degradation of the optics by damage or coating of the first optical component of the system does occur during the course of plasma campaigns. This is typically observed to be on the 10% level and, therefore, an additional 10% uncertainty is included in the absolute intensity calibrations of the diagnostic when analysing impurity densities. An absolute intensity calibration of both the entire system (optical head through to the spectrometer) and the spectrometer alone are performed such that the transmissions of the individual LOS (optical heads + relay fibers) can be determined independent of their position on the spectrometer. Here the transmission refers to the fraction of photons that are transmitted through the combination of the optical heads and the relay fibers. It does not include the spectrometers or spectrometer fibers. The transmissions of the system have a small wavelength dependence and vary from ~50% at 400nm to ~65% at 650nm. This information is useful for several reasons. First, it enables any changes in the intensity calibrations to be isolated to either the optical heads and relay-fibers or to the spectrometer and spectrometer fibres. These changes are tracked over multiple experimental campaigns and help us to identify problems and damaged components. Second, should the need arise, it enables us to change the connections of the relay fibers with respect to the spectrometer fibers (where a given LOS is measured on the camera), while maintaining the absolute intensity calibration to within the aforementioned 10-15%. Lastly, knowing the absolute intensity calibrations of the spectrometers alone, allows direct comparisons to be made between the various spectrometers installed at AUG.

Fig. 9 shows the spectrometer intensity calibrations for one of the new systems (COR F/2.8) in comparison to one of the older systems (CER F/4) as a function of channel on the CCD camera at a fixed wavelength. Both of these systems employ the same Princeton Instruments CCD chip. EM gain was not used for either set of data. In the case of the CER the controller gain was set to 2 and for the COR the controller gain was set to 4. Therefore, the data from the COR has been divided by 2 to enable a more direct comparison. Hence, these curves correspond to an effective controller gain of 2 for both systems. For otherwise identical cameras and settings, a factor of two improvement in intensity sensitivity was expected based on the $F/\#$ of the spectrometers. However, the measured intensities show on average less than this, only a factor of ~1.5 at the camera center increasing to ~1.8 near the edges of the camera due to the reduced vignetting with the larger lenses. It is not
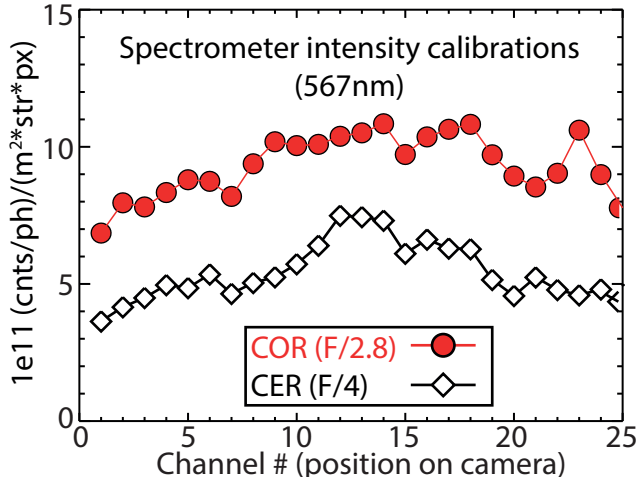
FIG. 9. Intensity calibrations of the new COR (F/2.8) spectrometer compared to the older CER (F/4) diagnostic as a function of position on the camera at fixed wavelength. Both systems feature identical cameras and no EM gain was used. The data shown here correspond to effective controller gains of 2 for both systems.

entirely clear where this "loss" of light originates. It is possible that the larger lenses have lower transmissions compared to those used in the F/4 systems.

IV. ANALYSIS OF CXRS SPECTRA

At AUG the majority of the plasma facing surfaces are either solid W or W-coated. There are no longer any graphite surfaces and the carbon content in the machine is typically 0.3% or less, making C CXRS measurements challenging. Therefore, the standard AUG CXRS impurity is boron, which is introduced into the machine through regular boronizations. Additional impurities, such as He, Li, C, N, O, F, Ne and Ar can be (and have been) measured with the core CXRS systems when these impurities are present in the machine. Typical B CXRS spectra from the COR diagnostic are shown in Fig. 10. Here, a spectrum from a LFS LOS around mid-radius, a LOS near the magnetic axis, and a HFS LOS also around mis-radius are shown. The standard fit recipe for the boron spectrum is comprised of 5 Gaussians, an active and passive line for both the n=7-6 and the n=11-8 BV transitions plus a single passive line for the edge BII emission line at 494.038nm. Here, active refers to emission that results from charge exchange reactions with the injected neutrals in the
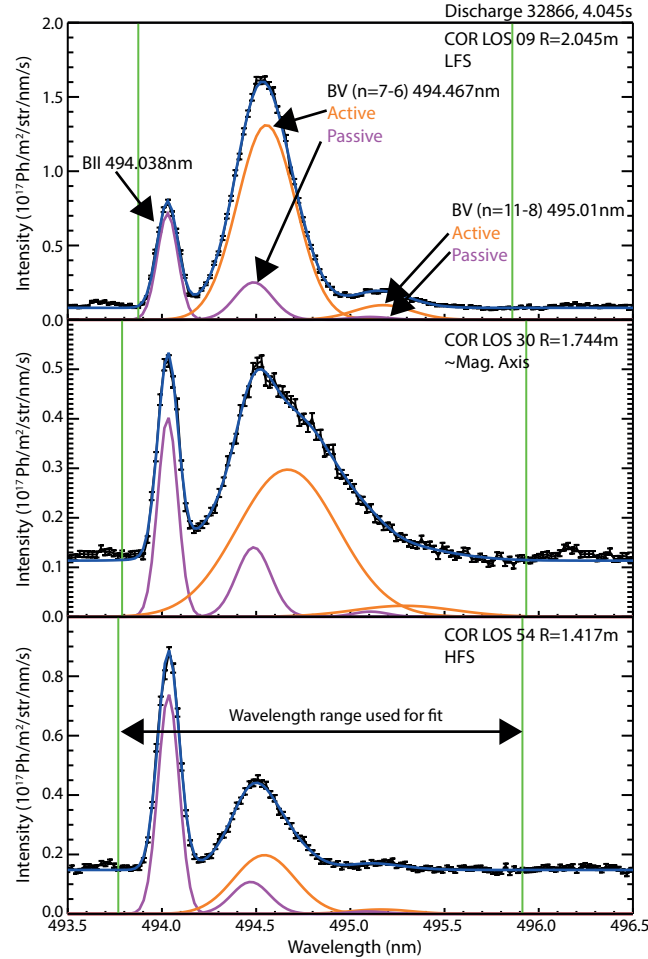
FIG. 10. Measured B spectra from the COR diagnostic taken in discharge 32866 at 4.045s. The top panel contains a spectrum from a LFS LOS around mid-radius, the middle panel a spectrum from near the magnetic axis, and the bottom panel a HFS spectrum from around mid-radius.

main plasma volume. Passive refers to emission from the plasma edge that originate due to electron impact excitation and other processes. The number of free parameters in this fit is reduced due to the fact that the temperatures and rotations derived from the n=7-6 and n=11-8 come from the same population of boron ions and, therefore, must be the same. In addition, the positions and widths of the passive contributions are constrained to reasonable temperature and rotation ranges consistent with the ionization stage of the impurity and its location in the plasma. These constraints help to correctly separate out the active and passive emissions. In all cases, the measured CXRS spectra are fit to a convolution of the Gaussians defined in the fit recipe and a Gaussian approximation to the instrument function (see previous section) for the corresponding spectrometer channel.
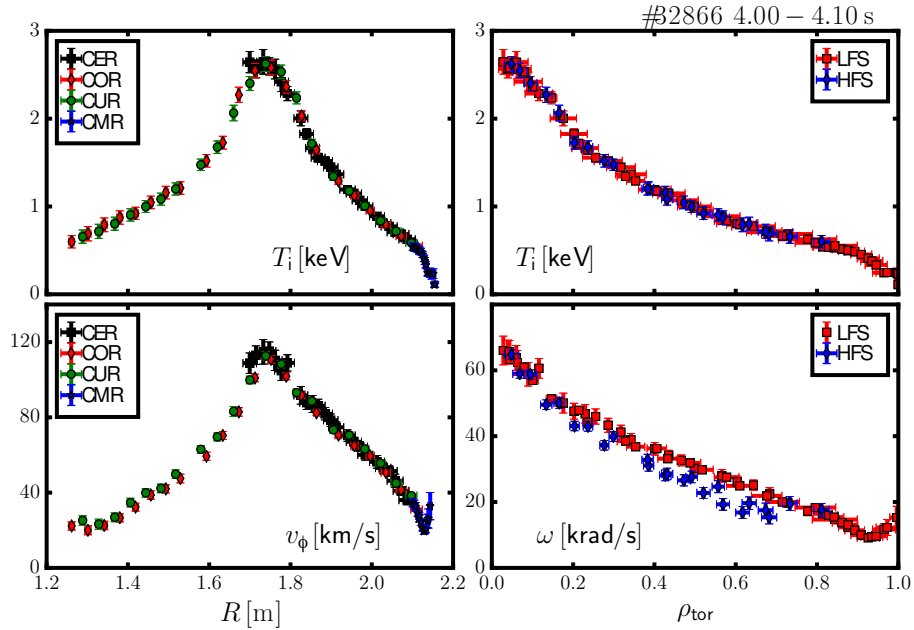
FIG. 11. Impurity ion temperature and toroidal rotation measured using the new and pre-existing CXRS diagnostics in discharges 32866 at 4.045s as a function of major radius (left) and mapped onto the normalized toroidal flux coordinate ρ_{tor} (right). The rotation shown on the left as a function of major radius is the rotation velocity in km/s, while on the right the toroidal rotation frequency $\omega = v_\phi/R$ is shown.

The full ion temperature and toroidal rotation profiles corresponding to these spectra are shown in Fig. 11. On the left hand side the profiles are shown as a function of major radius and the data from two pre-existing toroidal CXRS diagnostics from NBI 3 (CER in black squares and CMR in blue stars) are provided for comparison. The agreement between the diagnostics on the LFS is extremely good and one can see that the ion temperature profiles significantly constrain the position of the magnetic axis. On the right hand side, the same profiles are shown again as a function of the normalized toroidal flux coordinate, $\rho_{tor} = \sqrt{(\psi_0 - \psi)/(\psi_0 - \psi_{sep})}$. Here, the individual diagnostics are not distinguished. Rather, only whether the data was measured on the LFS (red squares) or on the HFS (blue diamonds) is indicated.

The HFS and LFS boron temperatures overlay extremely well. In this case, a pressure constrained equilibrium was used for the mapping. Without the pressure constraint, radial shifts of up 3 cm are required to align the HFS and LFS profiles, which is outside of the

19

error bars on the measurement. The relative alignment of the HFS and LFS T_i profiles, therefore, provides additional information on the magnetic flux surfaces, which can be used to check the quality of the equilibrium reconstruction.

Note that the diagnostic LOS are not purely in the toroidal direction, see Fig. 1, and, therefore, do not measure purely toroidal rotation. The vertical tilt angle of the LOS varies between 7 and 13 degrees with the largest angles for the LFS LOS (bottom head in Fig. 2) and the smallest for the HFS LOS. This means that if there is poloidal velocity in the plasma, these LOS pick up some projection of this flow. However, this projection is very small. Typical core poloidal velocities are on the order of 1km/s and the projection of this onto the LOS would result in a correction to the measured LOS velocities of 0.1-0.2 km/s. Core poloidal velocities of 10km/s and upwards would be needed before the projection of this velocity onto the LOS reached the uncertainty threshold of the measurement. Therefore, within the error bars, the LOS measured velocities represent the projection of the toroidal rotation into the LOS direction. Once the spectra are fit for the LOS velocities, the real plasma equilibrium is used to calculate the projection back into the purely toroidal direction for every LOS and every time frame.

Note that the rotation shown on the left-hand side of Fig. 11 is the toroidal rotation velocity (v_{tor}) in km/s, while on the right hand side, the toroidal rotation frequency $\omega = v_{tor}/R$ in kHz is shown. If the poloidal rotation in the plasma is zero, this quantity should be symmetric on a flux surface and the total plasma flow can be well described by simple solid body rotation. If the poloidal rotation is non-zero, however, then this will cause a poloidal asymmetry in the measured toroidal rotation frequency[4–6] from the LFS to the HFS. In the example shown here, one can see that the measured HFS frequency is slightly lower than the LFS frequency, indicating a small poloidal flow. Detailed calculations of the poloidal flow in the core of AUG plasmas using this method and comparisons to neoclassical theory will be the subject of an upcoming publications, and is beyond the scope of the work presented here.

The measured B^{+5} intensity profiles and corresponding impurity density profiles from the new and old CXRS diagnostics are shown in Fig. 12. Here, one can see that the intensities measured by the new (COR/CUR) and old (CER) diagnostics agree well. This is expected because, as previously mentioned, the difference in the charge exchange cross-sections for the 60 and 93KeV beams is compensated by the different number of particles
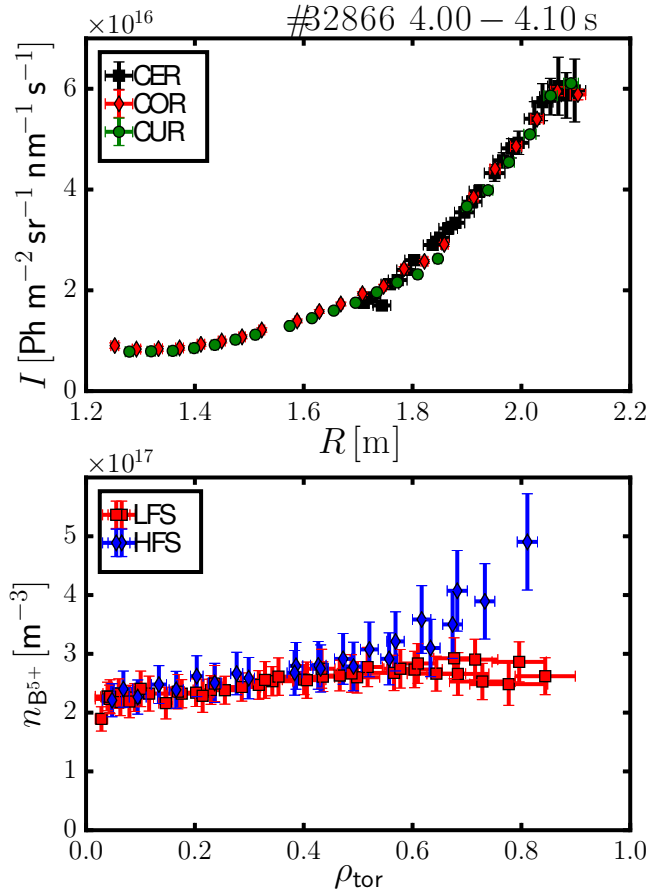
FIG. 12. (Top) Measured boron line intensities from the core CXRS diagnostics. (Bottom) Impurity density profiles calculated from both the CER (NBI 3, 60KeV) and the COR/CUR (NBI 8, 93keV) diagnostics.

injected by the different sources. The agreement in intensity between the two different sets of measurements provides an additional check on the intensity calibrations of the diagnostics and has been useful for identifying problems that occur during campaigns. The attenuation into the plasma for the two different beams, however, is different and this is reflected in the steeper attenuation observed for the CER (60KeV beam), which only just becomes visible near the plasma center.

The boron densities measured by the new and old diagnostics are shown in the bottom panel of Fig. 12. There is an asymmetry outside of ρ_ϕ=0.6, but inside of this radius the LFS and HFS density profiles overlay well. The good agreement between the calculated boron densities from the old and new CXRS diagnostics (all red squares) indicate that the intensity calibrations, the beam geometries for the two NBI boxes, the beam energy composition and

excited state calculations, and the neutral density attenuation calculations have all been implemented correctly.

Outside of $\rho_{tor} = 0.6$ the calculated HFS densities are larger than on the LFS. The reason for this is not yet known. However, it is a direct result of the slight increase in measured intensities that can be seen on the innermost points of Fig. 12. This asymmetry is not the result of errors in the intensity calibrations. Nor can it be explained by an incorrect beam geometry or beam attenuation. One possible explanation is that an additional unknown and unaccounted for emission in the measured spectrum could lead to an erroneous increased emission in this region. However, careful examination of the fitted spectra and the residuals show no evidence of this and, moreover, the asymmetry has been observed while measuring both boron and nitrogen. This makes an additional emission, which effects both spectral lines more or less identically in this region, very unlikely. Alternatively, the increased emission could be explained by an increased population of neutrals from the high field side SOL being transported inward and undergoing charge exchange reactions. This possibility will be tested in future experiments by using beam modulation to isolate the NBI-related active CXRS signal.

V.   ATOMIC EFFECTS ON THE CXRS SPECTRA

The LOS geometries of the new systems were optimised to maximise the radial resolution of the diagnostics (tangency to flux surfaces). This lead, however, to large angles between the LOS and the injection trajectory of the neutral beam varying from 76° on the LFS to 45° on the HFS. This can be seen, for example, in Fig. 1. Due to these angles and the energy dependence of the charge exchange cross-sections, the cross-section effects described in von Hellermann et al[13] need to be evaluated for each LOS and, when applicable, included in the analysis of the data. To evaluate the effect of cross-section effects on the measured spectra an approach similar to that described in von Hellermann et al was followed. The results of these calculations for the boron n=7-6 CX emission line are shown in Fig. 13. In the top plot the percent error between the true and the apparent impurity ion temperature $(\%\Delta_{T_i} = (T_{true} - T_{app})/T_{true} \times 100)$ is shown as a function of the true temperature for the COR LOS. The bottom curve (black) corresponds to the outermost LOS on the LFS and the top curve (red) to the innermost LOS on the HFS. Typically, the edge temperatures at

AUG are less than 1 keV, while core temperatures are typically less than 5 keV. However, for unusual cases core ion temperatures in the vicinity of 10 keV can be achieved. In all cases, the error on the ion temperature due to this effect remains less than 5% and has, therefore, not been included in the standard analysis.

For the rotation the cross-section effects can become important under certain circumstances. In the middle and bottom panels of Fig. 13 the percent error on the toroidal rotation as a function of ion temperature is shown for two different rotation velocities. At low rotation, significant corrections can become necessary at high ion temperatures. However, as the effect scales much more strongly with temperature than it does with the rotation velocity, the error on the measurement drops quickly with increased rotation. In the experiment, toroidal rotation and ion temperature are strongly correlated, meaning low rotation velocities typically only occur together with low ion temperatures and high velocities with high temperatures. Even for very high ion temperatures ($\sim$10 keV) in the plasma core, the effect remains under 10%. However, for the special circumstance of low rotation and high ion temperature, particularly on the HFS, these corrections should be considered.

These calculations are done considering only the first energy component of the beam, as this is the dominant contribution to the measured intensities. However, even small contributions from the lower beam energy components can potentially cause disproportionately large apparent velocities due to the increased slope of the charge exchange cross-section at lower energies for the standard CX transitions. For boron, the slope of the reaction rate is maximised around $\sim$25 keV/amu, which is quite close to the second energy population for NBI box II ($\sim$23 keV/amu). For the LFS LOS, the second energy component of the beam can be responsible for up to 25% of the total signal, while on the HFS, it is less than 10%. The cross-section effects on the measured CXRS spectra were also evaluated taking into account the contributions from the other neutral populations. To do this the charge exchange spectra, including cross-section effects, were calculated separately for each energy component as a function of true ion temperature and velocity and then weighted according to their contribution to the total CXRS signal and summed. The final resultant spectra were then fitted with single Maxwellians to determine the "total" cross-section effects on the measured spectra. While this procedure yields slightly larger differences between true and apparent temperature and rotations than if only the contribution from the first energy component is considered, the effects remain negligible for the typical range of AUG operation. Therefore,
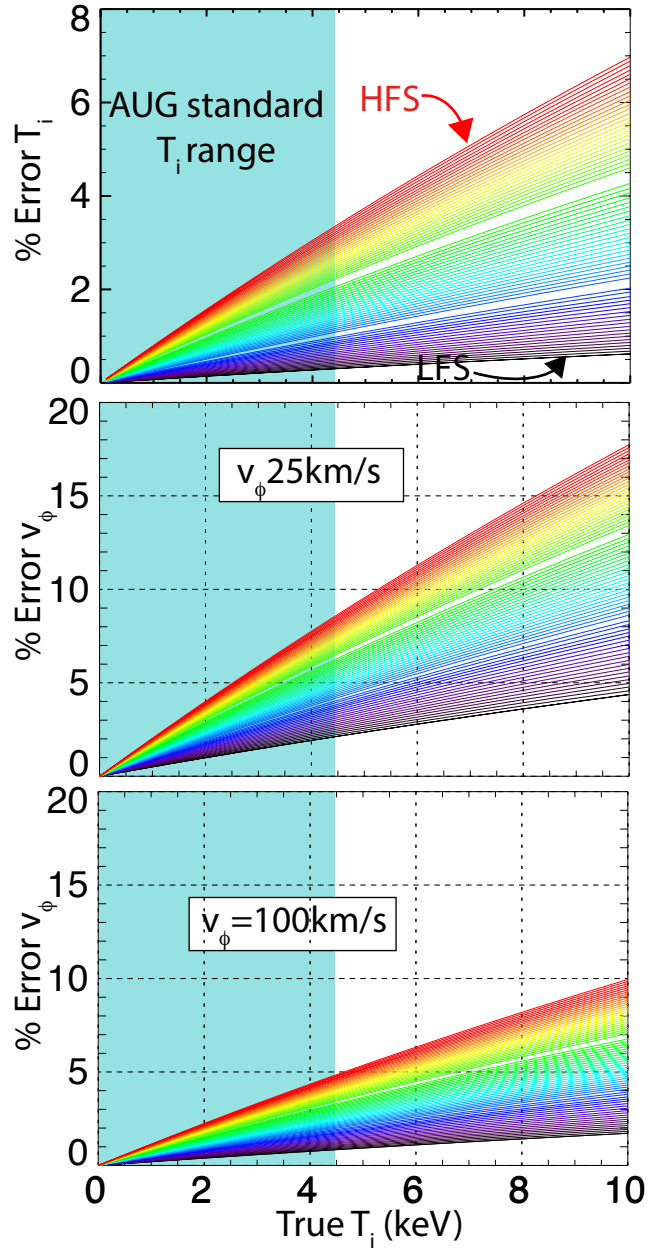
FIG. 13. Effect of the energy dependent charge exchange emission rates on the ion temperatures and toroidal rotations measured along the LOS of the new COR diagnostic. The apparent parameters here are calculated following the equations presented in von Hellermann *et al*[13] and taking into account only the first energy component of the beam. (Top) Percent error on the ion temperature and (Middle/Bottom) percent error on the toroidal rotation for two rotation values as a function of the true ion temperature. In all panels the bottom curve of each data set (black) corresponds to the outermost LOS on the LFS and the top curve (red) corresponds to the innermost LOS on the HFS.

these effects are not included in the routine data analysis.

It should be noted, however, that the cross-section effects on both T_i and v_ϕ are systematically higher for the HFS LOS than for the LFS LOS and this could potentially lead to systematic errors when using the LFS-HFS T_i data to constrain the magnetic equilibrium or using the LFS-HFS v_ϕ data to infer the core poloidal rotation. Therefore, cross-section effects are included in a post-processing analysis whenever the data is used for these purposes. In all cases considered to date, the cross-section induced differences in the measured LFS-HFS impurity ion temperatures have been found to be well within the error bars of the measurements and have not made a substantial impact on the reconstructed equilibrium. For extremely high temperature plasmas, however, this may not be the case. The reconstruction of the poloidal velocity relies on the absolute magnitude of the difference between the HFS and LFS toroidal rotation frequency, $\omega = v_\phi/R$. This means the differences in the toroidal rotation velocity induced by the cross-section effects is amplified by the difference in the major radii of the measurements on a given flux surface. For the evaluation of the poloidal rotation, the systematic error introduced by the cross-section effects has been found to be small, but not negligible, and is routinely included in all analyses of the poloidal rotation.

Gyro-orbit effects[14] on the measured spectra have been neglected as all of the LOS of this diagnostic are almost parallel to magnetic field lines within the neutral beam volume. However, it is necessary to correct for the Zeeman effect. The Zeeman effect causes a splitting of the spectral line when the atom is in the presence of a magnetic field. While this effect is typically small on AUG due to the relatively high ion temperatures (causing Doppler broadening to dominate over Zeeman splitting) and low magnetic fields, it is important for low temperature measurements, particularly on the HFS where the magnetic field can be up to 4T.

The measurements from all AUG CXRS diagnostics are corrected for Zeeman splitting and fine structure by means of correction curves. The full splitting (including Doppler) has been calculated for each measured impurity transition (B n=7-6, C n=8-7, ...) for a dense grid of magnetic fields, ion temperatures, and angles of the LOS with respect to the magnetic field. These spectra are then fit by a single Gaussian to determine the apparent ion temperature. In all cases, the final Zeeman broadened spectral line is found to fit well to a single Gaussian. After the experimental data is fit for the apparent temperature, the
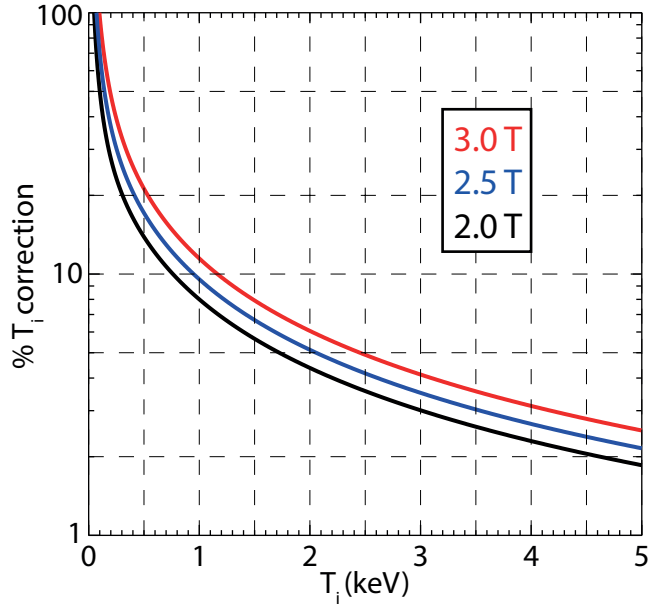
FIG. 14. Percent correction $((T_{i,app} - T_i)/T_i)$ to the apparent ion temperature as a function of true ion temperature for three magnetic field values. These curves are calculated for a LOS angle to the magnetic field of 15 degrees.

true temperature is determined by interpolation along these correction curves. In Fig. 14 the ion temperature corrections for three different magnetic field values corresponding to a LFS (2T), central (2.5T), and HFS (3T) location are shown as a function of true ion temperature for a LOS to field-line angle of 15 degrees. This is approximately the geometry of the LOS of the new diagnostics, the true angles of course vary slightly for each LOS and plasma equilibrium. For higher ion temperatures the Zeeman splitting causes a 5% or less correction to the apparent T_i. However, near the LFS and HFS pedestal tops the ion temperature can be between 500 and 1KeV. In this parameter regime the Zeeman effect can cause a 10-20% error and a LFS-HFS asymmetry on the order of 100 eV, if not properly taken into account.

VI. SUMMARY AND CONCLUSIONS

The existing suite of CXRS diagnostics at AUG has been extended to include a new core system that takes advantage of the higher neutral beam energies (93 keV) of NBI box II to measure across the magnetic axis onto the HFS. The new system features 70 lines of

sight (LOS) that image the full mid-plane of the plasma from the pedestal top on the LFS to the pedestal top on the HFS with an average channel to channel separation of 1.5 cm. Only 48 of these LOS are dedicated to CXRS. The other 22 are used for BES and provide measurements of the beam neutral densities along parallel LOS.

The fiber optics from the in-vessel optical heads are connected to two flexible wavelength spectrometers that have been optimised for light throughput and have been extensively calibrated for noise, wavelength, instrument functions, and absolute intensity. The CXRS LOS are split between the two spectrometers such that complete profiles, albeit at reduced radial coverage, of two separate impurity species can be measured at the same time. Or, more often, both systems measure a single impurity providing very detailed and complete profiles of that species. Typically, the new systems have sufficient signal to run at 10ms integration time and for special circumstances down to 2.5ms integration time.

These systems are capable of measuring the impurity ion temperature, toroidal rotation, and density on a shot-to-shot basis with between shot analysis when requested. The data is of higher quality than the pre-existing systems and reduces the error bars on the LFS measurements. Moreover, the data is of sufficiently high quality that the LFS-HFS ion temperature profiles provide an additional constraint on the magnetic equilibrium reconstruction and the poloidal rotation can be extracted from the observed poloidal asymmetries in the toroidal rotation frequency. Cross-section and other atomic effects on the measured spectra have been examined. While the fine structure and Zeeman splitting of the spectral lines is regularly included in the analysis via correction curves, both gyro-orbit effects and cross-section effects on the measured spectra were found to be negligible for typical AUG operating parameters and are not routinely included.

ACKNOWLEDGMENTS

REFERENCES

[1] R. J. Fonck, D.S. Darrow, and K. P. Jaehnig Determination of plasma-ion velocity distribution via charge-exchange recombination spectroscopy. Phys. Rev. A, 29(6):3288, 1984.

[2] R.C.Isler An overview of charge-exchange spectroscopy as a plasma diagnostic Plasma Phys. Control. Fusion, 36: 171-208 1994.

[3] E. Viezzer, T. Pütterich, R. Dux, R. M. McDermott and the ASDEX Upgrade Team. High-resolution charge exchange measurements at ASDEX Upgrade. Rev. Sci. Instrum., 83:103501, 2012

[4] A. Bortolon, Y. Camenen, A. N. Karpushov, B. P. Duval, Y. Andrebe, L. Federspiel, O. Sauter, and the TCV Team Indirect measurement of poloidal rotation using inboard-outboard asymmetry of toroidal rotation an comparison with neoclassical predictions. Nucl. Fusion., 53:023002, 2013

[5] C. Chrystal, K.H. Burrell, B.A. Grierson, L.L. Lao, D.C. Pace, Indirect measurement of poloidal rotation using inboard-outboard asymmetry of toroidal rotation an comparison with neoclassical predictions Rev. Sci. Instrum., 85:11E302, 2014

[6] K. Brau, M. Bitter, R. J. Goldston, D. and Manos, K. and McGuire, and S. Suckewer Plasma rotation in the PDX tokamak Nucl. Fusion, 23:1643, 1983

[7] R. Dux, B. Geiger, R. M. McDermott, T. Pütterich, E. Viezzer and the ASDEX Upgrade Team Impurity density determination using charge exchange and beam emission spectroscopy at ASDEX Upgrade 38th EPS Conference on Plasma Physics, Strasbourg, France 2011 available at: http://ocs.ciemat.es/EPS2011PAP/pdf/P1.056.pdf

[8] R. Dux, B. Geiger, R. M. McDermott, L. Menchero, T. Pütterich, E. Viezzer and the ASDEX Upgrade Team Impurity density determination using charge exchange and beam emission spectroscopy at ASDEX Upgrade 39th EPS Conference and 16th Int. Congress on Plasma Physics, Stockholm, Sweden, 2012 available at: http://ocs.ciemat.es/EPSICPP2012PAP/pdf/P2.049.pdf

[9] http://www.princetoninstruments.com

[10] A. D. Whiteford, M.G. von Hellermann, L. D. Horton, and K. D. Zastrow ADAS CXSFIT User Manual, available at: http://www.adas.ac.uk/notes/adas_r07-01.pdf, 2007.

[11] R. E. Bell Exploiting a transmission grating spectrometer Rev. Sci. Instrum., 75:4158-4161, 2004

[12] http://www.labsphere.com

[13] M. G. von Hellermann, P. Breger, J. Frieling, R. König, W. Mandl, A. and Maas, and H. P. Summers Analytical approximation of cross-section effects on charge exchange spectra observed in hot fusion plasmas <u>Plamsa Phys. and Control. Fusion</u>, 37:71-94, 1995

[14] R. E. Bell and E. Synokowski New understanding of poloidal rotation measurements in a tokamak plasma <u>AIP Conf. Proc.</u>, 39:547, 2000